Atmospheric source of mercury to the ocean constrained by isotopic model

Zhengcheng Song [1,2] ✉, Shaojian Huang[1], Yujuan Wang[1], Peng Zhang[1], Tengfei Yuan[3], Kaihui Tang[4], Xuewu Fu[4] & Yanxu Zhang [3] ✉

Mercury is a potent neurotoxin that poses significant health risks to humans, primarily through seafood consumption. Atmospheric deposition is the largest source of oceanic mercury, in either oxidized (Hg^{II}) or elemental (Hg^0) form. Understanding the relative contributions of atmospheric Hg^{II} and Hg^0 to the ocean is essential for accurately assessing global mercury budgets. Earlier even mercury isotope ($\Delta^{200}Hg$) analyses suggested equivalent Hg^{II}/Hg^0 contributions but neglected spatial variations in atmospheric $\Delta^{200}Hg$ signatures. Here, we developed a 3D atmospheric model incorporating mercury chemistry and isotopic fractionation to address this limitation. Our simulations reveal distinct atmospheric $\Delta^{200}Hg$ patterns and quantify their deposition to the ocean. Constrained by observed $\Delta^{200}Hg$ data in the ocean, we propose an updated deposition ratio of atmospheric Hg^{II} to Hg^0 to the ocean, which may exceed 2:1, higher than the previously reported 1:1. Our findings are crucial for assessing atmospheric mercury dispersal and predicting the recovery of marine ecosystems.

Mercury (Hg) is a pervasive global pollutant with severe health impacts[1]. It is released into the environment from both human activities, such as fossil fuel burning and mining, and natural processes like oceanic emissions and wildfires[2,3]. Once in the atmosphere, Hg exists mainly as gaseous elemental mercury (Hg^0), which makes up over 80% of atmospheric Hg and can remain airborne for months. The oxidized forms of mercury (Hg^{II}), including both gaseous [$Hg^{II}(g)$] and particle-bound species [$Hg^{II}(p)$], are less abundant but are rapidly removed by deposition[4–6]. Atmospheric deposition of Hg^{II} and Hg^0 represents the major source of Hg to marine environments, influencing Hg biomagnification and cycling in the ocean[7,8]. However, the precise contributions of these Hg forms to oceanic Hg levels remain uncertain.

Direct observations of Hg^0 and Hg^{II} deposition fluxes over the ocean are limited. Recent atmospheric model studies report varying ratios of Hg^{II} deposition compared to Hg^0 uptake overs ocean, accompanied by distinct Hg deposition fluxes. The models, including different assumptions in Hg emissions and atmospheric redox chemistry, indicated that Hg^{II} deposition over the modern ocean is 2:1 to 3:1

compared to Hg^0 uptake, with gross fluxes ranging from 3900 to 4600 Mg yr^{-1} and 1300 to 2000 Mg yr^{-1}, respectively[4,5]. These models are often evaluated against atmospheric Hg concentration data near the ground and the troposphere, as well as wet deposition fluxes observed over the land, leaving such a ratio largely unconstrained.

Isotopic signatures provide a more reliable means of constraining these fluxes. Mercury has seven isotopes that exhibit both mass-dependent (MDF, $\delta^{202}Hg$) and mass-independent fractionation (MIF) signatures, including odd-MIF ($\Delta^{199}Hg$ and $\Delta^{201}Hg$) and even-MIF ($\Delta^{200}Hg$ and $\Delta^{204}Hg$)[9,10]. Even-MIF is known to be generated in the upper troposphere through photochemical reactions, making it a conservative tracer in surface environments that can be used to trace atmospheric inputs of Hg^{II}[11–13]. A recent study by Jiskra et al.[14] compared atmospheric and marine $\Delta^{200}Hg$ signatures, suggesting an atmospheric Hg^{II}: Hg^0 contribution ratio of 1:1. This ratio is significantly lower than those reported in previous modeling studies. Based on this, a recent coupled atmosphere-land-ocean model updated the global Hg budget, suggesting a ratio of 1.5:1, but with much higher fluxes across the air-

[1]School of Atmospheric Sciences, Nanjing University, Nanjing, Jiangsu, China. [2]Frontiers Science Center for Critical Earth Material Cycling, Nanjing University, Nanjing, Jiangsu, China. [3]Department of Earth and Environmental Sciences, Tulane University, New Orleans, LA, USA. [4]State Key Laboratory of Environmental Geochemistry, Institute of Geochemistry, Chinese Academy of Sciences, Guiyang, China. ✉e-mail: songzc@nju.edu.cn; yzhang127@tulane.edu

sea interface, estimating Hg^{II} deposition and Hg^0 uptake at 4860 Mg yr^{-1} and 3270 Mg yr^{-1}, respectively[15].

However, most of the atmospheric isotope data used by Jiskra et al. [14] are derived from measurements on land or in coastal regions. Relying on land-based observations to trace oceanic Hg sources may introduce significant uncertainties. Firstly, previous observations and modeling have revealed substantial global spatial variation in atmospheric Hg isotopes[16–19]. Secondly, current isotopic observations primarily focus on Hg^0 and wet deposition, with a notable lack of isotopic characterization for dry deposition of Hg over the ocean. Accurate isotopic characterization of atmospheric end-members is crucial for effectively constraining sea-air Hg exchange using isotopes. But the absence of direct observations of Hg isotope signatures for different forms of Hg in the marine atmosphere limits the effectiveness of these constraints.

We propose that recent advancements in three-dimensional atmospheric Hg isotope modeling offer a promising opportunity to address this issue[18,19]. In this study, we aim to update the relative contributions of Hg^{II} and Hg^0 to oceanic Hg by using more accurate $\Delta^{200}Hg$ signatures in atmospheric end-members. We integrate Hg isotopes and isotopic fractionation into the GEOS-Chem model to develop an atmospheric Hg isotope model. Based on the even-MIF mechanisms outlined in our recent study (see Methods for details), we present an optimized modeling scenario for atmospheric even-MIF. This model elucidates the $\Delta^{200}Hg$ signatures in global atmospheric Hg deposition, constrained by observed $\Delta^{200}Hg$ in global atmospheric samples. By comparing these with observed oceanic $\Delta^{200}Hg$ values, we propose an updated ratio of atmospheric Hg^{II} to Hg^0 deposition to the ocean of over 2:1, higher than the previously reported 1:1 ratio. Our results indicate that spatial differentiation of atmospheric $\Delta^{200}Hg$ signatures significantly impacts the findings, with important implications for understanding the global Hg cycle.

Results and discussion

Model evaluation

We developed a three-dimensional isotopic model for atmospheric Hg, incorporating state-of-the-art Hg chemistry, to elucidate the potential processes driving even-MIF. Our model results show comparable spatial variability with globally observed Hg concentrations and wet deposition fluxes (Supplementary Discussion, Text1, Supplementary Fig. 1). Additionally, our modeling results reveal pronounced spatial variations in atmospheric $\Delta^{200}Hg$, particularly for Hg^{II} species, a phenomenon not previously documented (Fig. 1). Since the model outputs are annual averages, we utilize background observations, from various environments−including the poles, remote mountains, coastal regions, and marine boundary layer (MBL) areas−for modeling validation. The model results reproduce the observed $\Delta^{200}Hg$ signatures in global atmospheric samples, including Hg^0 (represented by $\Delta^{200}Hg^0$), $Hg^{II}(g)$ [represented by $\Delta^{200}Hg^{II}(g)$], $Hg^{II}(p)$ [represented by $\Delta^{200}Hg^{II}(p)$], and precipitation [represented by $\Delta^{200}Hg^{II}(pre)$]. As illustrated in Fig. 1a, the observed $\Delta^{200}Hg^0$ shows a mean value −0.07 ± 0.02‰ ($n = 48$), which is closely matched by modeled $\Delta^{200}Hg^0$ of −0.07 ± 0.01‰ ($n = 48$). The modeled mean $\Delta^{200}Hg^0$ also aligns with observations from the Arctic (about −0.07‰)[20–23], remote mountain regions (about −0.07‰)[11,24–26], and MBL (about −0.06‰)[27–30]. Similarly, the observed $\Delta^{200}Hg^{II}(p)$ has a mean value of 0.06 ± 0.05‰ ($n = 13$), and our model yields a consistent value of 0.06 ± 0.06‰ ($n = 13$) (Fig. 1b). Specifically, the model successfully reproduces the mean $\Delta^{200}Hg^{II}(p)$ values observed in remote mountain regions (about 0.10‰)[11,28,31,32] and coast MBL regions (about 0.06‰)[28,33–36], including the Huaniao Island (about 0.08‰) at Northwest Pacific Ocean[32].

The modeled $\Delta^{200}Hg^{II}(g)$ distribution closely mirrors that of $\Delta^{200}Hg^{II}(p)$ (Fig. 1c), which can be attributed to the degassing process that produces $Hg^{II}(g)$ from $Hg^{II}(p)$[4]. Although observations of $\Delta^{200}Hg^{II}(g)$ are limited, two studies have measured $\Delta^{200}Hg^{II}(g)$ in Grand

Bay, USA (0.18 ± 0.07‰)[34] and Pic du Midi, France (0.15 ± 0.06‰)[11], with our model yielding comparable mean values of 0.16‰ and 0.17‰, respectively. The modeled $\Delta^{200}Hg^{II}(pre)$ also exhibits a consistent mean value with observations, at 0.15 ± 0.04‰ ($n = 15$, Fig. 1d), and shows a significant positive correlation with observed data, with a correlation coefficient of 0.62, reproducing the latitudinal variation of observations (Fig. 1e). Notably, the modeled $\Delta^{200}Hg^{II}(pre)$ values (0.10‰ and 0.07‰) aligns well with observations from the Island of Hawaii (0.14 ± 0.05‰) and the R/V Kilo Moana (open ocean station ALOHA, 0.08‰)[37], which are representative of $\Delta^{200}Hg^{II}(pre)$ observed over the open Pacific Ocean. In summary, our model successfully simulates the gradient of $\Delta^{200}Hg$ values, with the highest values in precipitation samples, followed by $Hg^{II}(p)$, and the lowest in Hg^0. The close agreement between our modeled and observed values, which approximate a 1:1 relationship (Fig. 1f), underscores the reliable performance of our Hg isotope model.

The distinct variations in $\Delta^{200}Hg$ values among Hg^{II} species− including gaseous ($Hg^{II}(g)$), particulate ($Hg^{II}(p)$), and precipitation-derived ($Hg^{II}(pre)$)−arise from chemical fractionation processes. Comparison with the global atmospheric Hg redox rate (Supplementary Fig. 2a, d) reveals that regions dominated by net Hg oxidation, such as parts of the central Indian and Pacific Oceans, exhibit relatively lower $\Delta^{200}Hg$ values in $Hg^{II}(g)$, $Hg^{II}(p)$, and wet deposition (Fig. 1b, d). These patterns reflect the influence of specific fractionation mechanisms: Br-initiated oxidation dominates in the marine boundary layer (Supplementary Fig. 2a), while even-MIF processes occur during OH-initiated oxidation and $Hg^{II}(p)$ photoreduction (see Methods). Elevated $\Delta^{200}Hg^{II}$ values in African regions further highlight the spatial variability of chemical fractionation. High $PM_{2.5}$ concentrations driven by dust emissions (Supplementary Fig. 2e) promote $Hg^{II}(p)$ formation, while concurrent high photolysis frequencies (Supplementary Fig. 2f) induce strong net $Hg^{II}(p)$ reduction (Supplementary Fig. 2d). Additionally, significant OH-initiated chemical activity (Supplementary Fig. 2b) also contributes to this regional $\Delta^{200}Hg$ signal. We decompose the fractionation process and find that the OH-initiated chemistry and $Hg^{II}(p)$ photoreduction pathways induce distinct $\Delta^{200}Hg^{II}$ distribution patterns, as these reactions prevail in distinct atmospheric layers (Supplementary Fig. 3). Both processes contribute to the elevated $\Delta^{200}Hg^{II}$ values over the African landmass (Supplementary Fig. 3). The modeled $\Delta^{200}Hg^{II}$ signatures at the surface are also influenced by the upper atmosphere. The free troposphere, marked by intense redox rates[4,5] (Supplementary Fig. 2g and h), generates high $\Delta^{200}Hg$ values in Hg^{II} species (Supplementary Fig. 2f). Subsequent convective transport (Supplementary Fig. 4d, e) delivers these species to the surface, thereby affecting surface $\Delta^{200}Hg^{II}$ signatures. Moreover, compared with regions such as East and South Asia, the African region has relatively lower anthropogenic Hg emissions that is characterized with a close to zero $\Delta^{200}Hg$ signal, further enhancing the importance of chemical fractionation processes in this area.

Isotope signature of atmospheric deposition

The model elucidates the $\Delta^{200}Hg$ signatures of atmospheric sources deposited into the ocean, including Hg^0 uptake, Hg^{II} dry deposition, and Hg^{II} wet deposition. The $\Delta^{200}Hg$ signatures in deposited Hg are influenced by the corresponding signatures in atmospheric Hg. As shown in Fig. 2a, Hg^0 uptake by the ocean generally shows negative $\Delta^{200}Hg^0$ signatures, with a median value of −0.06‰ [interquartile range (IQR), −0.07‰ to −0.05‰]. In contrast, Hg^{II} dry deposition, encompassing both $Hg^{II}(g)$ and $Hg^{II}(p)$, displays distinct spatial variations in $\Delta^{200}Hg$ signatures (Fig. 2b). Globally, Hg^{II} dry deposition to the ocean has a median $\Delta^{200}Hg$ value of 0.00‰ (IQR, −0.02‰ to 0.03‰). And near-shore regions show higher $\Delta^{200}Hg$ values compared to the open ocean, with median values of 0.04‰ (IQR, 0.01‰ to 0.09‰) and 0.01‰ (IQR, −0.01‰ to 0.03‰), respectively. The modeled $\Delta^{200}Hg$ values in wet deposition to the ocean are generally positive, with a
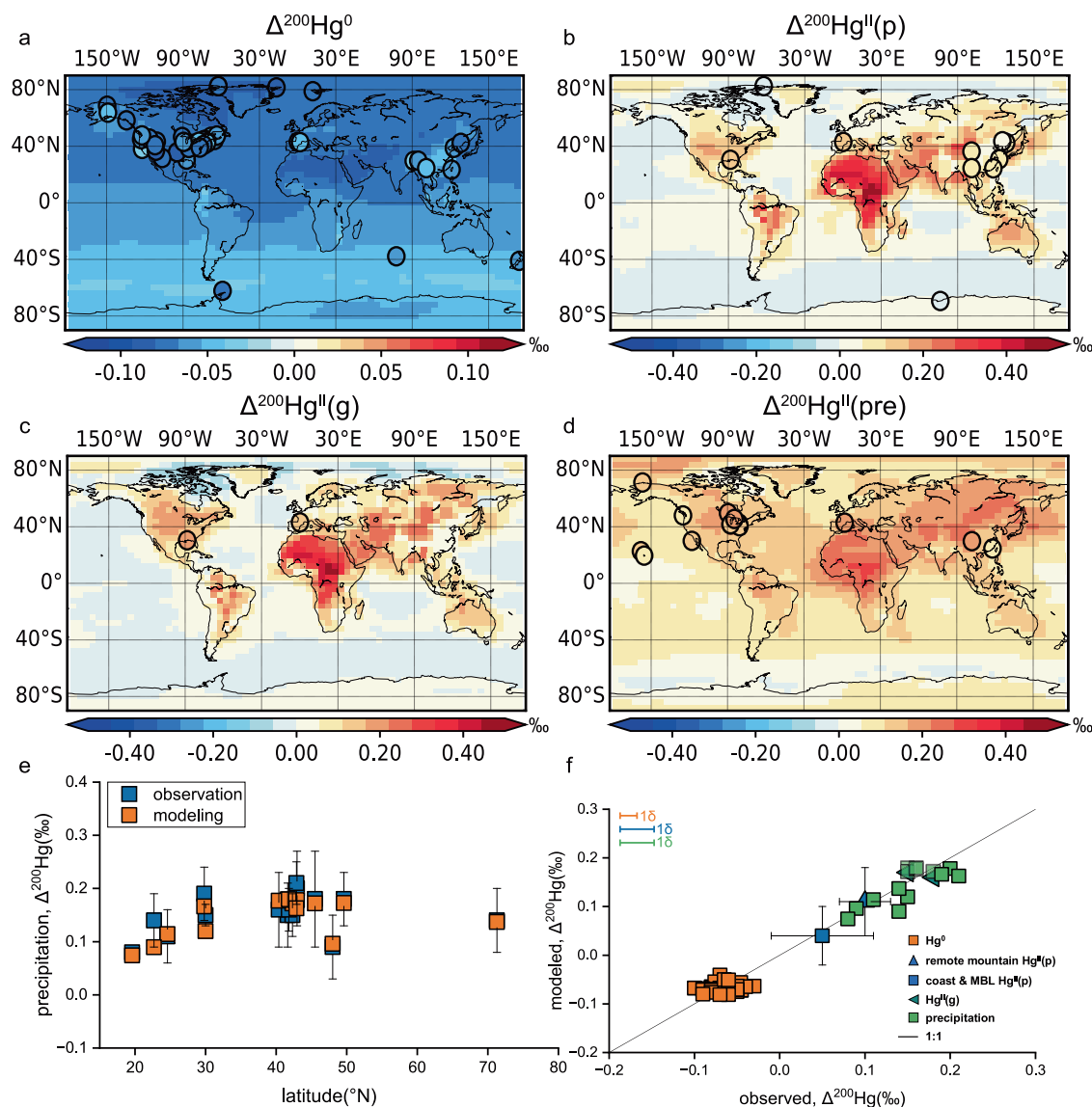
Fig. 1 | Distribution patterns of modeled $\Delta^{200}Hg$ signatures in surface atmosphere. a Comparison of modeled and observed $\Delta^{200}Hg^0$ values. **b** Comparison of modeled and observed $\Delta^{200}Hg^{II}(p)$ values. **c** Comparison of modeled and observed $\Delta^{200}Hg^{II}(g)$ values. **d** Comparison of modeled and observed $\Delta^{200}Hg^{II}(pre)$ values. The circles and the color they carry represent the location and the $\Delta^{200}Hg$ values of observations, respectively. **e** Comparison of simulated and observed latitudinal $\Delta^{200}Hg$ signatures in precipitation. The green and red squares represent

observations and modeling data, respectively. **f** Comparison of observed and modeled annual mean $\Delta^{200}Hg$ values in atmospheric samples. The abbreviation MBL represents the marine boundary layer. Error bars represent the reported stand deviation of measured $\Delta^{200}Hg$ for: Hg^0 (yellow), $Hg^{II}(g)$ (blue), and wet-deposited Hg^{II}(green) (1δ). Error bars for $Hg^{II}(p)$ represent spatial variability in observational and modeled datasets (1δ).

median of 0.08‰ (IQR, 0.06‰ to 0.12‰) for the global ocean and 0.11‰ (IQR, 0.09‰ to 0.13‰) for near-shore regions (Fig. 2c). The spatial patterns in both dry and wet deposition display similar trends, largely driven by the $\Delta^{200}Hg^{II}$ distributions (Fig. 1 and Supplementary Fig. 4). Although Hg^{II} dry deposition occurs primarily in the boundary layer, the $\Delta^{200}Hg$ signatures of $Hg^{II}(g)$ and $Hg^{II}(p)$ therein are significantly influenced by upper-atmospheric processes—similar to the $\Delta^{200}Hg$ observed in precipitation due to the washout of Hg^{II} species from higher altitudes. Moreover, elevated $\Delta^{200}Hg$ values in both dry and wet deposition near coastal regions are also influenced by terrestrial transport, as on-land Hg chemistry exhibits stronger reduction rates (Supplementary Fig. 2), leading to higher $\Delta^{200}Hg$ in Hg^{II} species.

Our results reveal distinct differences between the $\Delta^{200}Hg$ signatures of atmospheric dry deposition Hg^{II} and wet deposition Hg^{II} over the ocean—a detail not fully emphasized in previous studies[14]. Since dry deposition of Hg^{II} occurs primarily in the boundary layer,

while wet deposition of Hg^{II} originates mainly from higher atmospheric layers, the $\Delta^{200}Hg$ values for wet deposition are considerably higher than those for dry deposition. In Jiskra's study[14], the $\Delta^{200}Hg$ characteristics of dry- and wet-deposited Hg^{II} were not distinguished; instead, they were combined into a Hg^{II} end-member with $\Delta^{200}Hg$ values ranging from 0.13‰ to 0.15‰. Compared to our modeling results, this approach likely overestimates the $\Delta^{200}Hg$ of the dry deposition Hg^{II}, leading to an underestimation of Hg^{II} deposition's contribution to oceanic Hg. Our model provides more detailed $\Delta^{200}Hg$ signatures of atmospheric Hg sources, offering a more accurate resolution of the contribution of atmospheric Hg to oceanic Hg.

Atmospheric sources to ocean

We use $\Delta^{200}Hg$ data to evaluate the atmospheric contribution of Hg to the ocean, as $\Delta^{200}Hg$ is uniquely produced in the atmosphere and remains conserved in ocean. We exclude other potential marine Hg

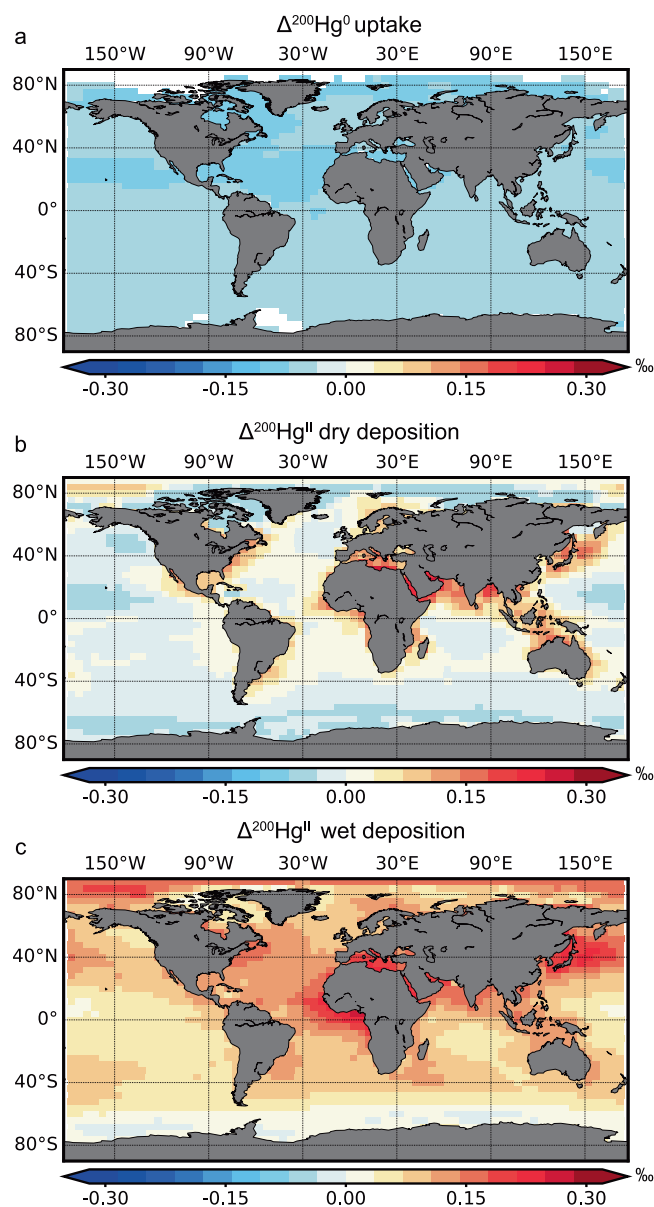**Fig. 2 | Annual mean Δ^{200}Hg signatures of atmospheric Hg deposited to the ocean. a** Δ^{200}Hg in Hg^0 uptake by the ocean. **b** Δ^{200}Hg in the dry deposition of Hg^{II}, including both direct deposition and uptake by sea salt. **c** Δ^{200}Hg in the wet deposition of Hg^{II}. Hg^0 uptake by the ocean is calculated using Eqs. (1) and (2) as described in "Method" section, representing the uptake of atmospheric Hg^0. Hg^{II} deposition includes both dry and wet deposition of Hg^{II}(g) and Hg^{II}(p).

sources, such as hydrothermal emissions and river inputs, since hydrothermal Hg flux is minimal[38] and riverine Hg primarily affects coastal regions[39]. Figure 3a compares the modeled latitudinal variations of Δ^{200}Hg in atmospheric Hg depositions with observations in ocean samples (see method). The deposited Δ^{200}Hg values exhibit three different gradients, with wet deposition showing the highest values, followed by Hg^{II} dry deposition, and then Hg^0 uptake. The observed interquartile ranges (P25–P75) of Δ^{200}Hg values in ocean samples fall between these three end-members of Hg depositions, suggesting that the relative proportions of these three depositions to oceanic Hg can be differentiated based on Δ^{200}Hg isotope mass balance.

The Δ^{200}Hg^0 values exhibit minimal variation with latitude, with only a slight downward trend observed in lower latitudes (Fig. 3a). In contrast, Δ^{200}Hg in both dry and wet deposition of Hg^{II} shows distinct latitudinal variations, with an increasing trend in low-latitude regions. This corresponds with an upward trend in oceanic Δ^{200}Hg values in the same areas, suggesting a greater contribution of atmospheric Hg^{II} to oceanic Hg compared to atmospheric Hg^0. Additionally, both Hg^0 and dry-deposited Hg^{II} display lower Δ^{200}Hg values compared to observed values in certain regions, such as between 20°S and 40°S and 50°N and 70°N, indicating a more significant role for wet deposition in these areas. The overall Δ^{200}Hg values in both wet and dry deposition of Hg^{II} align more closely with observed oceanic Δ^{200}Hg, indicating that atmospheric Hg^{II} might be a more substantial contributor to the global ocean Hg pool than atmospheric Hg^0.

The Hg deposition proportions and isotopic signatures of this model can be further used to quantify the contribution of atmospheric Hg to marine Hg. As illustrated in Fig. 3b, the majority of Δ^{200}Hg values in the modeled total atmospheric deposition (purple area) are comparable to the interquartile range of oceanic observations. This suggests that the relative proportions of the three types of Hg deposition in our model are largely reasonable for explaining the oceanic Δ^{200}Hg. However, the modeled Δ^{200}Hg values are also slightly lower than the observations between 20°S to 40°S, 10°N to 20°N, and 50°N to 70°N, implying a potential underestimation of the relative contribution from Hg^{II} wet deposition or, alternatively, an overestimation of Hg^0 uptake and Hg^{II} dry deposition in these regions. Indeed, previous studies have shown that the GEOS-Chem model underestimates Hg^{II} precipitation in equatorial tropical areas, partly due to its limitations in accurately predicting cloud mass in these regions[7,40]. Additionally, when combined our modeled Δ^{200}Hg with Jiskra's Hg deposition flux data[14], the total Δ^{200}Hg also shows lower values in the regions between 20°S to 40°S and 50°N to 70°N (Supplementary Fig. 5), further supporting this conclusion.

Figure 3c exhibits the proportions of the three types of depositions to the ocean calculated by the model. The proportion of Hg^0 tends to decrease in low-latitude tropical regions, while the proportion of Hg^{II} wet deposition tends to increase. This trend may explain why ocean samples from these regions exhibit higher Δ^{200}Hg values (Fig. 3a), as wet deposition in these areas is associated with high positive Δ^{200}Hg values (Fig. 3b). Globally, atmospheric Hg^0 contributes 34% to oceanic Hg, while atmospheric Hg^{II} accounts for the remaining 66%, with 38% from dry deposition and 28% from wet deposition. This indicates a 2:1 ratio of atmospheric Hg^{II} to Hg^0 deposition over the ocean. Given the potential underestimation of wet deposition's contribution in the model as indicated above, we suggest this ratio likely exceeds 2:1, significantly higher than the 1:1 ratio reported in the previous study[14]. This also implies that the contribution of atmospheric Hg^{II} wet deposition to marine Hg may be greater than 28%, suggesting that the combined contribution of Hg^{II} dry deposition and Hg^0 uptake could be less than 72%.

Uncertainty
The uncertainties in this study may stem from the simulation of even-MIF of atmospheric Hg. While our model can replicate Δ^{200}Hg values comparable to atmospheric observations, the fractionation mechanisms and enrichment factors for even-MIF in the model have not been definitively established. Therefore, we advocate for further experimental and theoretical investigations on this matter. Additionally, the Hg isotope signatures of source emissions exhibit standard deviations ranging from 0.02‰ to 0.05‰, as indicated in Table 1. To evaluate the impact of the upper and lower bounds (maximum or minimum isotopic composition) of various emission sources on the modeling results, we performed a sensitivity analysis. The findings indicate that uncertainties in source emissions can lead to shifts of ±0.02‰ to ±0.03‰ in the simulated Δ^{200}Hg^0, Δ^{200}Hg^{II}(g), Δ^{200}Hg^{II}(p), and Δ^{200}Hg^{II}(pre), which minimally impact the analysis of these Δ^{200}Hg values. Another uncertainty arises from the assumption that all oceanic Hg originates from the atmosphere, which may not be applicable to
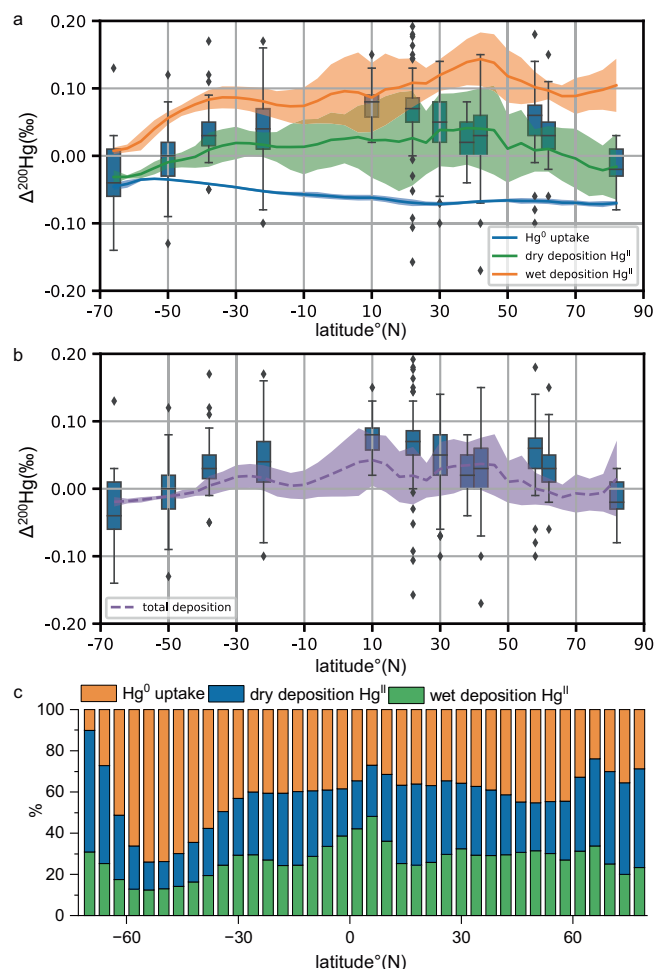
Fig. 3 | Comparison of Δ^{200}Hg signatures in modeled atmospheric mercury deposition versus measured oceanic samples. a Latitudinal variation of Δ^{200}Hg values in atmospheric deposited Hg and oceanic Hg. The boxes represent Δ^{200}Hg observations (interquartile range, P25–P75) in ocean samples, including seawater, particle-bound Hg, sediment, and biota[14], aggregated by contiguous latitudes. The bold line in boxes represents the median, the boxes represent the IQR, the whiskers represent 1.5× the IQR, and outliers are represented by dots. The yellow line indicates modeled Δ^{200}Hg signatures in Hg^0 uptake by the ocean. The green and red lines represent modeled Δ^{200}Hg signatures in dry and wet deposition Hg^{II} over the ocean. The shaded area represents the standard deviation of the latitudinal mean. **b** Comparison of Δ^{200}Hg values in modeled total deposited Hg with ocean observations. The pink dotted line and shaded area represent the modeled Δ^{200}Hg signatures and standard deviation of total Hg deposited from the atmosphere to the ocean, encompassing Hg^0 uptake, dry deposition of Hg^{II}, and wet deposition of Hg^{II}. **c** Modeled fraction of the three categories of depositions relative to total atmospheric Hg deposition to the ocean.

coastal regions where rivers are the predominant source[39]. Uncertainties may also result from the limited observational coverage of the ocean. Current observations do not encompass the entire ocean, particularly in open ocean regions like the central Indian Ocean and the Pacific Ocean. This uneven spatial distribution of observations may influence the analysis of the results.

Another source of uncertainty arises from the delineation of the Hg cycle of our isotope model. However, the impact on our conclusion is limited as the simulation of deposition fluxes and their isotopes in our model operates relatively independently. To validate this, we conducted sensitivity tests using different enrichment factors (E^{200}Hg) during the chemical fractionation process. As illustrated in Supplementary Fig. 6, two scenarios with various E^{200}Hg yielded consistent ratios of the three forms of Hg occupancy, although the simulated

Δ^{200}Hg values varied significantly. Moreover, the isotopic observations in atmospheric and ocean samples are independent of the simulations, providing robust constraints on the modeled Δ^{200}Hg signatures in both atmospheric Hg and its deposition. This confirms the feasibility of using modeled Δ^{200}Hg values to trace oceanic Hg sources.

The modeling uncertainties may arise from the omission of the lightning process that induces even-MIF, as proposed by recent experimental studies[41]. As a result, this could influence the simulation of Δ^{200}Hg signatures in wet deposition, given that precipitation events are often associated with lightning. However, according to Sun et al.[41], it is still unrealistic to attribute global significance to Hg(^{3}P)-induced oxidation (Supplementary Discussion, Text S2). Another potential source of bias is the model resolution. For example, the 4° × 5° GEOS-Chem model may fail to accurately capture high-altitude precipitation events in North America[42], potentially leading to an underestimation of Hg elution with positive Δ^{200}Hg^{II} values from higher altitudes in this region. Additionally, although the model reproduces the existing observations well, these are primarily concentrated in East Asia, North America, Europe, and parts of the Arctic. Consequently, we recommend that future studies focus on more remote regions, such as South America, Africa, and the open ocean.

Implications
Current observations lack the direct measurement of fluxes in both Hg^{II} and Hg^0 deposition over the ocean. The Δ^{200}Hg data and modeling indicate that previous findings, which suggested an equal contribution (1:1) of atmospheric Hg^{II} and Hg^0 to the ocean[14], may be biased. Our analysis proposes a higher relative contribution of Hg^{II}, with a ratio of might over 2:1, and highlights the significant spatial heterogeneity of Δ^{200}Hg in atmospheric Hg deposition as a key factor in resolving isotopic signatures at the Earth's surface, including both land and ocean. The greater relative contribution of atmospheric Hg^{II} to marine Hg may impact the marine ecosystems, as various forms of Hg in the ocean affect methylmercury production[43,44]. This has direct implications for human health due to the consumption of seafood containing methylmercury. Conversely, since Hg^0 constitutes the majority of atmospheric Hg, its smaller relative contribution to oceanic Hg affects its atmospheric lifetime and ultimately influences the benefits of reducing anthropogenic Hg emissions.

The updated ratio provides an important constraint for the global Hg budget, offering insights into the sea-air Hg fluxes. In global modeling studies, sea-air exchange fluxes can be adjusted within the model by modifying relevant parameters to achieve a self-consistent Hg balance between sea and air[4,5,15]. For example, a coupled atmosphere-land-ocean model[15] suggests atmospheric Hg^0 and Hg^{II} deposition fluxes of 3270 Mg yr^{-1} and 4860 Mg yr^{-1}, respectively, constrained by the previously believed 1:1 Hg^{II} to Hg^0 ratio. This indicates an ocean Hg^0 emission of 7220 Mg yr^{-1} resulted from adapting faster air-sea exchange velocities. Our study suggests that the oceanic Δ^{200}Hg data may not fully support this budget.

Our results effectively differentiate the spatial variation of Δ^{200}Hg in atmospheric Hg and distinguish between the Δ^{200}Hg signatures of dry and wet deposition over the ocean. This demonstrates the advantages of three-dimensional atmospheric Hg isotope modeling, which effectively captures global variations in atmospheric Hg isotopes, compensates for the inhomogeneity of observational data, and provides new perspectives on using Hg isotopes to analyze the global Hg cycle. To better constrain the global Hg cycle, we propose that both atmospheric and oceanic Hg balance and isotopic composition should be integrated. Future research should focus on developing coupled atmosphere-land-ocean isotope models, which could serve as a powerful tool for constraining the global Hg cycle.

Methods
Model description
The GEOS-Chem (version 12.9.0) platform is used to develop the Hg isotope model, featuring a resolution of 4° latitude by 5° longitude and

Table 1 | Mercury flux and Δ^{200}Hg signatures of source emissions

Sources	Anthropogenic[a]	Soil[b]	Ocean[c]	Biomass[d]	Geogenic[e]
Flux (Mg y^{-1})	2200	850	4800	300	300
Δ^{200}Hg(‰)$_{mean}$	0.00	−0.01	0.04	−0.04	0.00
1sd	0.03	0.03	0.05	0.02	0.02

The fluxes of Hg emission sources are from Shah et al.[4].
[a]The isotope signatures of anthropogenic emission are cited from Sun et al.[66,67].
[b]Δ^{200}Hg emission from soil is adopted from Sun et al.[67] and Wang et al.[68].
[c]We estimate the Δ^{200}Hg emission from ocean is consistent with that in oceanic samples[14].
[d]Δ^{200}Hg in biomass emission are compiled from refs. 21,25,28,69–71.
[e]Δ^{200}Hg in geogenic emission are adopted from volcanic emission reported by Sun et al.[66].

47 vertical layers[18,19]. The model employs the native MERRA-2 (4° × 5°) meteorological reanalysis data produced by NASA's Global Modeling and Assimilation Office (GMAO). Anthropogenic Hg emissions are sourced from Streets et al.[45], while natural emissions are cited from Shah et al.[4]. Atmospheric Hg^{II}, including Hg^{II}(g) and Hg^{II}(p), experiences both dry and wet deposition over the ocean. Dry deposition of Hg following the resistance-in-series scheme of Wesely (1989)[46]. Over the ocean, dry deposition velocity for the atmospheric Hg^{II}(g) is biologically unreactive and has a highly high Henry's law constant[47]. Dry deposition of Hg^{II}(p) is calculated according to the aerosol deposition scheme[48,49]. Sea-salt aerosol uptake of Hg^{II} also acts as a dry deposition sink of Hg in the marine boundary layer[6]. And wet scavenging of Hg^{II} follows the scheme proposed by Amos et al.[50] and Liu et al.[51]. The exchange of Hg^0 between the air-sea interface is controlled by the following equations[48]:

$$Flux_{-up} = K_w \times CHg_0 \tag{1}$$

$$Flux_{-down} = K_w \times CHg_a / H \tag{2}$$

Where Flux$_{up}$ represents the flux of Hg^0 from the ocean to the atmosphere, and K$_w$ denotes the mass transfer coefficient, which was developed based on field experiments with volatile and nonvolatile tracers[52]. CHg$_0$ is the concentration of dissolved Hg^0 in seawater. We utilize the state-of-the-art chemistry mechanism of atmospheric Hg, which includes mainly four redox pathways[4]: (i) the oxidation of Hg^0 to Hg^{II} by Br; (ii) the oxidation of Hg^0 to Hg^{II} by OH; (iii) the oxidation of Hg^0 to Hg^{II} by Cl; (iv) photoreduction of Hg^{II}(p) to Hg^0. This mechanism also integrates the photoreduction of gaseous Hg^{II}[53], a process that occurs primarily within the Br-initiated pathway and significantly influences global Hg deposition. The oxidant field includes debromination from sea-salt aerosol in the marine atmosphere[54,55], which enhances the Br radicle concentration in the marine boundary compared to previous Br fields[56]. The model simulation covers the period from 2016 to 2018, with the first two years used for model initialization and the third year dedicated to result analysis.

Isotope notion and fractionation

We follow the notation established by Blum and Bergquist[10] to express the modeled isotope signatures. These notations are defined as the isotopic ratio difference simulated species and the NIST-3133 standard, measured in permil (‰):

$$\delta^{xxx}Hg(‰) = [(^{xxx/198}Hg/^{xxx/198}Hg_{NIST3133}) - 1] \times 1000 \tag{3}$$

MIF is calcuated as below:

$$\Delta^{199}Hg = \delta^{199}Hg - \delta^{202}Hg \times 0.252 \tag{4}$$

$$\Delta^{200}Hg = \delta^{200}Hg - \delta^{202}Hg \times 0.502 \tag{5}$$

$$\Delta^{201}Hg = \delta^{201}Hg - \delta^{202}Hg \times 0.752 \tag{6}$$

$$\Delta^{204}Hg = \delta^{204}Hg - \delta^{202}Hg \times 1.493 \tag{7}$$

In our calculations, the $^{xxx/198}$Hg$_{NIST3133}$ ratios are treated as constants, derived from the atomic abundances of Hg isotopes in the NIST-3133 standard[10,57]: ^{196}Hg = 0.155%, ^{198}Hg = 10.04%, ^{199}Hg = 16.94%, ^{200}Hg = 23.14%, ^{201}Hg = 13.17%, ^{202}Hg = 29.73%, and ^{204}Hg = 6.83%. For the Hg isotope inventories, we synthesize the Hg isotopic composition of each source and calculate its isotopic ratio ($^{xxx/198}$Hg) using Eqs. (3)–(7) (Table 1). These ratios allow us to divide total Hg emissions into seven isotopes, which can be input into the model as individual tracers. After running the model, it outputs the concentrations and fluxes of these isotopes, enabling us to calculate the isotope signatures using Eqs. (3)–(7).

Our model incorporates isotopic fractionation during chemical processes, treating these fractionations as kinetic processes. The chemical reaction coefficients are slightly adjusted for various isotopes by applying multiple fractionation factors (α), thus achieving isotope fractionation during these chemical reactions[18,19]. In the model, ^{198}Hg is treated as the reference isotope, maintaining the chemical reaction coefficients (K$_{198}$) consistent with the standard GEOS-Chem. The calculations of K$_{xxx}$ for other six isotopes follow the MDF kinetic laws and utilizes reported enrichment factors for specifically processes. The K$_{xxx}$ is for calculating K$_{xxx}$ is as follows:

$$\ln(\alpha^{xxx/198}Hg_{MDF}) = \varepsilon^{xxx}Hg/1000 \tag{8}$$

$$\ln(\alpha^{xxx/198}Hg_{MIF}) = E^{xxx}Hg/1000 \tag{9}$$

$$\ln(\alpha^{xxx/198}Hg_{MDF}) = \beta_{xxx} \times \ln(\alpha^{202/198}Hg) \tag{10}$$

$$\alpha^{xxx/198}Hg_{tot} = \alpha^{xxx/198}Hg_{MDF} \times \alpha^{xxx/198}Hg_{MIF} \tag{11}$$

$$K_{xxx} = K_{198} \times \alpha^{xxx/198}Hg_{tot} \tag{12}$$

Where the ε^{xxx} and E^{xxx} represent the reported enrichment factors for MDF and MIF, respectively. These factors are calculated as the difference between the MDF and MIF signatures as product over reactant Hg pool. The calculation of $\alpha^{xxx/198}$Hg$_{MDF}$ follows the kinetic laws governing Hg transfer, where β takes values as −0.507, 0.252, 0.502, 0.752, and 1.493 for ^{196}Hg, ^{199}Hg, ^{200}Hg, ^{201}Hg, ^{202}Hg, and ^{204}Hg, respectively[10]. The $\alpha^{xxx/198}$Hg$_{tot}$ represents the processes-based kinetic fractionation factors and is defined as the ratio of $^{xxx/198}$Hg for the product to that in the reactant. The $\alpha^{xxx/198}$Hg$_{tot}$ comprises two parts: $\alpha^{xxx/198}$Hg$_{MDF}$ and $\alpha^{xxx/198}$Hg$_{MIF}$.

In this study, we focus on the mass-independent fractionations of even mass isotopes (represented by Δ^{200}Hg). While previous studies[11–13,41,58] have documented elevated Δ^{200}Hg values in precipitation and aerosols, the mechanisms driving even-MIF remain poorly constrained. Chemical processes of Hg^0 photo-oxidation in the

tropopause[12,13] and Hg^{II} photolysis on aerosols mediated by magnetic halogen nuclei[11] have been proposed as potential sources. Experimental evidence further implicates mercuric oxide photodissociation in UVC-exposed $Hg–O_2$ systems[41]. Recent detections of positive $\Delta^{200}Hg$ in high-altitude gaseous $Hg^{II}(g)$, particulate Hg ($Hg^{II}(p)$), and marine/urban aerosols[59–63] underscore the spatial complexity of these processes. Here, we evaluate atmospheric Hg redox pathways using the state-of-the-art atmospheric Hg chemical frameworks[4], identifying $Hg^{II}(p)$ photoreduction and OH-initiated reactions are plausible dominant even-MIF drivers. Our model successfully reproduces global $\Delta^{200}Hg$ distributions (Supplementary Discussion Text S2), resolving key uncertainties in the environmental contexts and chemical pathways of even-MIF generation.

Mercury isotope data

We synthesized representative atmospheric observations of $\Delta^{200}Hg$. These observations are far away from high anthropogenic emission areas, especially for East Asia, where the atmospheric $\Delta^{200}Hg$ signatures are significant influenced by anthropogenic emissions. The selected observations are conducted at poles, remote mountain regions, coast areas, marine boundary layer. Most of the land-based observations are from Asia and North America and are presented as average values, including Hg^0, $Hg^{II}(p)$, and precipitation [$Hg^{II}(pre)$] samples. All the atmospheric isotope data are presented in Supplementary Table 1. For oceanic Hg isotopic signatures, we utilize the synthesized data from Jiskra et al. [14], which includes total Hg in seawater, particle-bound Hg, sediment, and biota samples. These data are collected from four oceans: the Mediterranean Sea, Atlantic Ocean, Pacific Ocean, and Southern Ocean. The median $\Delta^{200}Hg$ for oceanic samples are as follows: 0.03‰ (IQR, 0.01‰ to 0.05‰; $n = 87$) for the Mediterranean Sea, 0.02‰ (IQR, −0.01‰ to 0.05‰; $n = 122$) for the Atlantic Ocean, 0.06‰ (IQR, 0.03‰ to 0.08‰; $n = 295$) for the Pacific Ocean, 0.00‰ (IQR, −0.03‰ to 0.08‰; $n = 110$) for the Southern Ocean. All $\Delta^{200}Hg$ signatures for various sample categories in the oceans are detailed in Jiskra et al. [14].

Data availability

All data generated in this study are available in the main text, the supplementary information, and the research group website: https://www.ebmg.online/mercury. The data for model evaluation are synthesized from references and presented in Supplementary Information/Source data file. Source data are provided with this paper.

Code availability

In adherence to principles of transparency and reproducibility, we have made our code accessible to facilitate the replication and validation of our findings. All Hg isotope model code is available at the research group website (https://www.ebmg.online/mercury)[64]. The original GEOS-Chem code can be obtained at: https://github.com/geoschem/geos-chem (https://doi.org/10.5281/zendo.15242410)[65].

References

1. Zhang, Y. et al. Global health effects of future atmospheric mercury emissions. *Nat. Commun.* **12**, 3035 (2021).
2. Obrist, D. et al. A review of global environmental mercury processes in response to human and natural perturbations: changes of emissions, climate, and land use. *Ambio* **47**, 116–140 (2018).
3. Sonke, J. E. et al. Global change effects on biogeochemical mercury cycling. *Ambio* **52**, 853–876 (2023).
4. Shah, V. et al. Improved mechanistic model of the atmospheric redox chemistry of mercury. *Environ. Sci. Technol.* **55**, 14445–14456 (2021).
5. Horowitz, H. M. et al. A new mechanism for atmospheric mercury redox chemistry: implications for the global mercury budget. *Atmos. Chem. Phys.* **17**, 6353–6371 (2017).
6. Holmes, C. D. et al. Global atmospheric model for mercury including oxidation by bromine atoms. *Atmos. Chem. Phys.* **10**, 12037–12057 (2010).
7. Zhang, Y. et al. A coupled global atmosphere-ocean model for air-sea exchange of mercury: insights into wet deposition and atmospheric redox chemistry. *Environ. Sci. Technol.* **53**, 5052–5061 (2019).
8. Zhang, Y., Jaeglé, L. & Thompson, L. Natural biogeochemical cycle of mercury in a global three-dimensional ocean tracer model. *Glob. Biogeochem. Cycles* **28**, 553–570 (2014).
9. Blum, J. D., Sherman, L. S. & Johnson, M. W. Mercury isotopes in earth and environmental sciences. *Annu. Rev. Earth Planet. Sci.* **42**, 249–269 (2014).
10. Blum, J. D. & Bergquist, B. A. Reporting of variations in the natural isotopic composition of mercury. *Anal. Bioanal. Chem.* **388**, 353–359 (2007).
11. Fu, X. et al. Mass-independent fractionation of even and odd mercury isotopes during atmospheric mercury redox reactions. *Environ. Sci. Technol.* **55**, 10164–10174 (2021).
12. Cai, H. M. & Chen, J. B. Mass-independent fractionation of even mercury isotopes. *Sci. Bull.* **61**, 116–124 (2016).
13. Chen, J. B., Hintelmann, H., Feng, X. B. & Dimock, B. Unusual fractionation of both odd and even mercury isotopes in precipitation from Peterborough, ON, Canada. *Geochim. Cosmochim. Acta* **90**, 33–46 (2012).
14. Jiskra, M. et al. Mercury stable isotopes constrain atmospheric sources to the ocean. *Nature* **597**, 678–682 (2021).
15. Zhang, Y. et al. An updated global mercury budget from a coupled atmosphere-land-ocean model: 40% more re-emissions buffer the effect of primary emission reductions. *One Earth* **6**, 316–325 (2023).
16. Kwon, S. Y. et al. Mercury stable isotopes for monitoring the effectiveness of the Minamata Convention on Mercury. *Earth Sci. Rev.* **203**, https://doi.org/10.1016/j.earscirev.2020.103111 (2020).
17. Tsui, M. T.-K., Blum, J. D. & Kwon, S. Y. Review of stable mercury isotopes in ecology and biogeochemistry. *Sci. Total Environ.* **716**, https://doi.org/10.1016/j.scitotenv.2019.135386 (2020).
18. Song, Z. C., Huang, S. J., Zhang, P., Yuan, T. F. & Zhang, Y. X. Isotope data constrains redox chemistry of atmospheric mercury. *Environ. Sci. Technol.* **58**, 13307–13317 (2024).
19. Song, Z., Sun, R. & Zhang, Y. Modeling mercury isotopic fractionation in the atmosphere. *Environ. Pollut.* 119588, https://doi.org/10.1016/j.envpol.2022.119588 (2022).
20. Jiskra, M., Sonke, J. E., Agnan, Y., Helmig, D. & Obrist, D. Insights from mercury stable isotopes on terrestrial–atmosphere exchange of Hg(0) in the Arctic tundra. *Biogeosciences* **16**, 4051–4064 (2019).
21. Obrist, D. et al. Tundra uptake of atmospheric elemental mercury drives Arctic mercury pollution. *Nature* **547**, 201–204 (2017).
22. Zheng, W. et al. Mercury stable isotopes reveal the sources and transformations of atmospheric Hg in the high Arctic. *Appl. Geochem.* **131**, https://doi.org/10.1016/j.apgeochem.2021.105002 (2021).
23. Araujo, B. F. et al. Mercury isotope evidence for Arctic summertime re-emission of mercury from the cryosphere. *Nat. Commun.* **13**, 4956 (2022).
24. Wu, X. et al. Changes in atmospheric gaseous elemental mercury concentrations and isotopic compositions at Mt. Changbai during 2015–2021 and Mt. Ailao during 2017–2021 in China. *J. Geophys. Res. Atmos.* **128**, https://doi.org/10.1029/2022jd037749 (2023).
25. Kurz, A. Y., Blum, J. D., Gratz, L. E. & Jaffe, D. A. Contrasting controls on the diel isotopic variation of Hg(0) at two high elevation sites in the Western United States. *Environ. Sci. Technol.* **54**, 10502–10513 (2020).
26. Enrico, M. et al. Atmospheric mercury transfer to peat bogs dominated by gaseous elemental mercury dry deposition. *Environ. Sci. Technol.* **50**, 2405–2412 (2016).

27. Nguyen, L. S. P., Sheu, G.-R., Fu, X., Feng, X. & Lin, N.-H. Isotopic composition of total gaseous mercury at a high-altitude tropical forest site influenced by air masses from the East Asia continent and the Pacific Ocean. *Atmos. Environ.* **246**, https://doi.org/10.1016/j.atmosenv.2020.118110 (2021).

28. Fu, X. et al. Isotopic composition of gaseous elemental mercury in the marine boundary layer of East China Sea. *J. Geophys. Res. Atmos.* **123**, 7656–7669 (2018).

29. Szponar, N. et al. Isotopic characterization of atmospheric gaseous elemental mercury by passive air sampling. *Environ. Sci. Technol.* **54**, 10533–10543 (2020).

30. Li, C. et al. A peat core Hg stable isotope reconstruction of Holocene atmospheric Hg deposition at Amsterdam Island (37.8oS). *Geochim. Cosmochim. Acta* **341**, 62–74 (2023).

31. Fu, X. et al. Isotopic compositions of atmospheric total gaseous mercury in 10 Chinese cities and implications for land surface emissions. *Atmos. Chem. Phys.* **21**, 6721–6734 (2021).

32. Fu, X. et al. Domestic and TRansboundary Sources of Atmospheric Particulate Bound Mercury in Remote Areas of China: Evidence from Mercury Isotopes. *Environ. Sci. Technol.* **53**, 1947–1957 (2019).

33. Sun, L. et al. Mercury concentration and isotopic composition on different atmospheric particles (PM10 and PM2.5) in the subtropical coastal suburb of Xiamen Bay, Southern China. *Atmos. Environ.* **261**, https://doi.org/10.1016/j.atmosenv.2021.118604 (2021).

34. Rolison, J. M., Landing, W. M., Luke, W., Cohen, M. & Salters, V. J. M. Isotopic composition of species-specific atmospheric Hg in a coastal environment. *Chem. Geol.* **336**, 37–49 (2013).

35. Yu, B. et al. New evidence for atmospheric mercury transformations in the marine boundary layer from stable mercury isotopes. *Atmos. Chem. Phys.* **20**, 9713–9723 (2020).

36. Li, C. J. et al. Seasonal variation of mercury and its isotopes in atmospheric particles at the Coastal Zhongshan Station, Eastern Antarctica. *Environ. Sci. Technol.* **54**, 11344–11355 (2020).

37. Motta, L. C. et al. Mercury cycling in the North Pacific subtropical gyre as revealed by mercury stable isotope ratios. *Glob. Biogeochem. Cycles* **33**, 777–794 (2019).

38. Torres-Rodriguez, N. et al. Mercury fluxes from hydrothermal venting at mid-ocean ridges constrained by measurements. *Nat. Geosci.* **17**, 51–57 (2023).

39. Liu, M. et al. Rivers as the largest source of mercury to coastal oceans worldwide. *Nat. Geosci.* **14**, 672–677 (2021).

40. Soerensen, A. L. et al. Elemental mercury concentrations and fluxes in the tropical atmosphere and ocean. *Environ. Sci. Technol.* **48**, 11312–11319 (2014).

41. Sun, G. et al. Dissociation of mercuric oxides drives anomalous isotope fractionation during net photo-oxidation of mercury vapor in air. *Environ. Sci. Technol.* **56**, 13428–13438 (2022).

42. Xu, X. et al. Modeling the high-mercury wet deposition in the southeastern US with WRF-GC-Hg v1.0. *Geosci. Model Dev.* **15**, 3845–3859 (2022).

43. Zhang, Y. X., Soerensen, A. L., Schartup, A. T. & Sunderland, E. M. A global model for methylmercury formation and uptake at the base of marine food webs. *Glob. Biogeochem. Cycles* **34**, e2019GB006348 (2020).

44. Wu, P. & Zhang, Y. Toward a global model of methylmercury biomagnification in marine food webs: trophic dynamics and implications for human exposure. *Environ. Sci. Technol.* https://doi.org/10.1021/acs.est.3c01299 (2023).

45. Streets, D. G. et al. Global and regional trends in mercury emissions and concentrations, 2010–2015. *Atmos. Environ.* **201**, 417–427 (2019).

46. Wesely, M. L. Parameterization of surface resistances to gaseous dry deposition in regional-scale numerical-models. *Atmos. Environ.* **23**, 1293–1304 (1989).

47. Feinberg, A., Dlamini, T., Jiskra, M., Shah, V. & Selin, N. E. Evaluating atmospheric mercury (Hg) uptake by vegetation in a chemistry-transport model. *Environ. Sci. Process Impacts* https://doi.org/10.1039/d2em00032f (2022).

48. Strode, S. A. et al. Air-sea exchange in the global mercury cycle. *Glob. Biogeochem. Cycles* **21**, https://doi.org/10.1029/2006gb002766 (2007).

49. Zhang, L., Gong, S., Padro, J. & Barrie, L. A size-segregated particle dry deposition scheme for an atmospheric aerosol module. *Atmos. Environ.* **35**, 549–560 (2001).

50. Amos, H. M. et al. Gas-particle partitioning of atmospheric Hg(II) and its effect on global mercury deposition. *Atmos. Chem. Phys.* **12**, 591–603 (2012).

51. Liu, H. Y., Jacob, D. J., Bey, I. & Yantosca, R. M. Constraints from Pb-210 and Be-7 on wet deposition and transport in a global three-dimensional chemical tracer model driven by assimilated meteorological fields. *J. Geophys. Res. Atmos.* **106**, 12109–12128 (2001).

52. Nightingale, P. D. et al. In situ evaluation of air-sea gas exchange parameterizations using novel conservative and volatile tracers. *Glob. Biogeochem. Cycles* **14**, 373–387 (2000).

53. Saiz-Lopez, A. et al. Photoreduction of gaseous oxidized mercury changes global atmospheric mercury speciation, transport and deposition. *Nat. Commun.* **9**, 4796 (2018).

54. Wang, X. et al. Global tropospheric halogen (Cl, Br, I) chemistry and its impact on oxidants. *Atmos. Chem. Phys.* **21**, 13973–13996 (2021).

55. Wang, X. et al. The role of chlorine in global tropospheric chemistry. *Atmos. Chem. Phys.* **19**, 3981–4003 (2019).

56. Schmidt, J. A. et al. Modeling the observed tropospheric BrO background: Importance of multiphase chemistry and implications for ozone, OH, and mercury. *J. Geophys Res. Atmos.* **121**, 11819–11835 (2016).

57. Blum, J. D. in *Handbook of Environmental Isotope Geochemistry* Ch. Chapter 12, 229-245 (2012).

58. Bergquist, B. A. in *Encyclopedia of Engineering Geology Encyclopedia of Earth Sciences Series* Ch. Chapter 122-1, 1-7 (2018).

59. Liu, C. et al. Sources and transformation mechanisms of atmospheric particulate bound mercury revealed by mercury stable isotopes. *Environ. Sci. Technol.* **56**, 5224–5233 (2022).

60. AuYang, D. et al. South-hemispheric marine aerosol Hg and S isotope compositions reveal different oxidation pathways. *Nat. Sci. Open*, https://doi.org/10.1051/nso/2021001 (2022).

61. Qiu, Y. et al. Identification of potential sources of elevated PM2.5-Hg using mercury isotopes during haze events. *Atmos. Environ.* **247**, https://doi.org/10.1016/j.atmosenv.2021.118203 (2021).

62. Qiu, Y. et al. Stable mercury isotopes revealing photochemical processes in the marine boundary layer. *J. Geophys. Res. Atmos.* https://doi.org/10.1029/2021jd034630 (2021).

63. Huang, S. et al. Evidence for mass independent fractionation of even mercury isotopes in the troposphere. *Atmos. Chem. Phys. Discuss.* **2022**, 1–42 (2022).

64. Song, Z. et al. Atmospheric source of mercury to the ocean constrained by isotopic model. Hg-isotope modeling. Available at: http://www.ebmg.online/mercury/ (2025).

65. The International GEOS-Chem User Community. geoschem/geoschem: GEOS-Chem 14.6.0 (14.6.0). Zenodo. https://doi.org/10.5281/zenodo.15242410. (2025)

66. Sun, R. et al. Historical (1850–2010) mercury stable isotope inventory from anthropogenic sources to the atmosphere. *Elementa Sci. Anthr.* **4**, https://doi.org/10.12952/journal.elementa.000091 (2016).

67. Sun, R. et al. Modelling the mercury stable isotope distribution of Earth surface reservoirs: Implications for global Hg cycling. *Geochim. Cosmochim. Acta* **246**, 156–173 (2019).

68. Wang, X. et al. Climate and vegetation as primary drivers for global mercury storage in surface soil. *Environ. Sci. Technol.* **53**, 10665–10675 (2019).

69. Jiskra, M. et al. Mercury deposition and Re-emission pathways in boreal forest soils investigated with Hg isotope signatures. *Environ. Sci. Technol.* **49**, 7188–7196 (2015).

70. Yu, B. et al. Isotopic composition of atmospheric mercury in Cchina: new evidence for sources and transformation processes in air and in vegetation. *Environ. Sci. Technol.* **50**, 9262–9269 (2016).

71. Wang, X. et al. Global warming accelerates uptake of atmospheric mercury in regions experiencing glacier retreat. *Proc. Natl. Acad. Sci. USA* **117**, 2049–2055 (2020).

Acknowledgements

Author contributions

Conceptualization: Z.S., Y.Z., S.H. Methodology: Z.S., Y.W., Z.P., T.Y., K.T., X.F. Investigation: Z.S., S.H., T.Y. Visualization: Z.S., S.H. Funding acquisition: Z.S. Project administration: Z.S., Y.Z. Supervision: Z.S., Y.Z. Writing—original draft: Z.S., Y.Z., X.F. Writing—review and editing: Z.S., Y.Z., X.F., K.T., S.H., T.Y., Y.W.

Competing interests

The authors declare no competing interests.

Additional information

Correspondence and requests for materials should be addressed to Zhengcheng Song or Yanxu Zhang.